Controllable Crystallization Optimizes Thermal Stability of A Novel Red-emitting Phosphor in Self-reduction System

LU Shiwei[1], DONG Rui[1], BAI Yuxing[1], DU Haihong[1], ZHENG Lirong[2],
WU Li[1*], KONG Yongfa[1], XU Jingjun[1]

（1. *The MOE Key Laboratory of Weak Light Nonlinear Photonics*，*School of Physics*，*Nankai University*，*Tianjin* 300071，*China*；
2. *Beijing Synchrotron Radiation Facility*，*Institute of High Energy Physics*，*Chinese Academy of Sciences*，*Beijing* 100049，*China*）

∗ *Corresponding Author*，*E-mail*：*lwu@nankai. edu. cn*

Abstract：Thermal quenching（TQ）at elevated temperature is a major factor affecting the luminescent intensity and efficiency of phosphors. Improving the thermal stability of phosphors and weakening the TQ effect are of significance for the high-quality illumination of phosphor-converted WLEDs. Here，a novel red-emitting phosphor $K_2Zn(PO_3)_4$：Mn^{2+} is synthesized by standard high temperature solid state reaction in ambient atmosphere，which is a new member of self-reduction system. An effective synthesis strategy is proposed to optimize its photoluminescent performances. Combined with X-ray photoelectron spectroscopy and X-ray absorption fine structure spectroscopy，oxygen vacancy defects introduced by Mn doping are proved to play an important role in the transition of $Mn^{4+} \rightarrow Mn^{2+}$. Thermoluminescence analysis reveals that the distribution of trap levels，especially the deep ones，is effectively regulated by the controllable crystallization and significantly affect the thermal stability of phosphors. Then a defect-assisted model is proposed to address the inner mechanism of the phenomenon. The carriers trapped by deep trap levels can be released under the high-temperature stimulus，which return back to the luminescent centers and participate in the radiative recombination to improve thermal stability. This study provides a new crystallographic idea and theoretical support for obtaining luminescent materials with high thermal stability.

Key words：photoluminescence；lattice defects；self-reduction；thermal stability

可控结晶法优化一种自还原体系新型红色荧光粉的热稳定性

鹿诗为[1]，董　瑞[1]，白宇星[1]，杜海红[1]，郑黎荣[2]，武　莉[1*]，
孔勇发[1]，许京军[1]

（1. 南开大学 物理科学学院，弱光非线性光子学教育部重点实验室，天津　300071；
2. 中国科学院高能物理研究所 北京同步辐射装置，北京　100049）

摘要：高温下热猝灭(TQ)是影响荧光粉发光强度与发光效率的主要因素。提高荧光粉的热稳定性、减少热猝灭对于光转换型白光 LED 的高质量照明至关重要。本文报道了一种新型红色荧光粉 $K_2Zn(PO_3)_4$：Mn^{2+}，该材料以标准高温固相法在空气中合成，属自还原体系。同时，提出了一种有效合成策略优化其发光性能。结合 X 射线光电子能谱和 X 射线吸收精细结构谱，证实 Mn^{2+} 掺杂引入的氧空位缺陷在锰离子价态转移过程中起

重要作用。热释光分析表明,可控结晶过程有效地调节了深陷阱能级的分布,显著提高了荧光粉的热稳定性。本文提出了一种缺陷辅助模型来解释这一现象的内在机理。深陷阱能级俘获的载流子在高温刺激下释放,返回发光中心并参与辐射复合,进而提高荧光粉的热稳定性。该研究为获得高热稳定性荧光粉提供了新的晶体学思路和理论支持。

关 键 词: 光致发光;晶体缺陷;自还原;热稳定性

1　Introduction

The fourth-generation solid-state lighting technology based on the phosphor-concerted white light emitting diodes (pc-WLEDs) is rapidly developing in indoor and outdoor lighting, liquid crystal display backlights, information recording, and storage, *etc*.[1-3]. At present, the common method to manufacture prototypes is coating phosphors onto LED chips, and generates a broad emission band covering the entire visible gamut by down-conversion[4-6]. Though functional, the drawbacks like low color rendering index (R_a) and high correlated color temperature (CCT) are also quite obvious to restrict their extensive development[7-9]. Accordingly, a high-performance pc-WLED with high R_a and low CCT should be expected to meet the particular illumination requirements, of which the key relies on the performances of phosphors, especially at high temperatures[10-12]. The high-temperature photoluminescence behavior of blue- and green-emitting phosphors is mostly satisfied, such as $BaMgAl_{10}O_{17}:Eu^{2+}$ and $(Ba,Sr)_2SiO_4:Eu^{2+}$[13-14], while that of red-emitting phosphors remains a big challenge, such as $Ca_4LaO(BO_3)_3:Eu^{3+}$ and $LiNa_2B_5P_2O_{14}:Eu^{3+}$[15-16]. Therefore, it is critical to develop the red luminescence materials with excellent thermal stability for improving the performance of pc-WLEDs.

Then extensive efforts have been made to optimize the high-temperature performance of red-emitting phosphors, such as nitrides $Sr_{1.98-x}(Ca_{0.55}Ba_{0.45})_xSi_5N_8:Eu_{0.02}$ and $CaAlSiN_3:Eu^{2+}$[17-18]. Mn^{4+}-doped fluoride-based materials have also attracted attention due to their outstanding properties, like $K_2TiF_6:Mn^{4+}$ and $Rb_2CsSiF_7:Mn^{4+}$[19-20]. Despite the good thermal stability, the preparation conditions of high temperature and pressure are necessary for the aforementioned hosts. In addition, part of the activator ions obtained from reducing atmosphere are prone to be re-oxidized at elevated-temperature running environment, leading to chromaticity coordinate deviation. Therefore, it is exciting to obtain the excellent phosphors by mild synthesis condition and long-term stabilized low-valence activators without reducing atmosphere, namely killing two birds with one stone. So the self-reduction system would be an ideal choice, such as $NaZn(PO_3)_3:Mn^{2+}$ and $LiZnPO_4:Mn^{2+}$[21-24]. However, not all the self-reduction phosphors show good thermal stability because of the unpredictable position of defect levels. Then the position adjustment of defect level is undoubtedly an effective way to improve their thermal stability. Unlike the cationic substitution methods, which have been proven to be effective to regulate defect positions, from a crystallographic perspective, the crystallization process of compounds can also greatly affect the position of defect levels[25-27]. Based on that, changing the preparation conditions of the samples will be a feasible strategy to obtain the positive response of optical properties to defect control.

Here in this work, we come up with an effective strategy of changing crystallization condition to improve the thermal stability of a new red-emitting phosphor $K_2Zn(PO_3)_4:Mn^{2+}$, which is successfully synthesized by high-temperature solid-state reaction method in an ambient atmosphere. A self-reduction phenomenon of Mn^{4+} to Mn^{2+} ions is realized and attributed to the existence of V_O. By adjusting the sintered time (24 h), the deep trap levels are regulated to locate in a suitable position in the forbidden band, which facilitates the improvement of thermal stability. The mechanism of improved thermal stability is studied and explained by a defect-assisted model in detail. This study provides an effective crystallographic method for regulating the position of defect levels.

2　Experiment

2.1　Materials Synthesis

　　A series of phosphors $K_2Zn_{1-x}(PO_3)_4$：xMn^{2+} (x = 0.01－0.15 mol, named as KZPOM$_x$ in the following text) were synthesized by the high-temperature solid-state reaction method in an ambient atmosphere. Initial reactants were K_2CO_3（≥99%）, ZnO（≥ 99%）, $NH_4H_2PO_4$（≥99%）, and MnO_2（≥97.5%）, which were mixed homogeneously and ground thoroughly in an agate mortar for 30 min. After fully grinding, the mixtures were respectively sintered in air at 500 ℃ for 17, 24, 36, 48 h.

2.2　Characterization

　　The phases of the obtained samples were identified by X-ray powder diffraction（Bruker-D8 AD-VANCE, Bruker, Germany）with Cu Kα radiation at a scanning time of 0.10 s operating at 40 kV and 40 mA. Phases of the as-prepared phosphors samples were identified by Inorganic Crystal Structure Database（ICSD #166829）. The XRD data for structural refinements were collected over a 2θ range from $10°$ to $140°$ at intervals of $0.02°$ with a counting time of 0.5 s per step using the software TOPAS. The XAFS spectra were measured by means of the 1W1B beamline（Beijing Synchrotron Radiation Facility）using transmission mode, and the energy was adjusted *via* a Mn metal foil. The XAFS data were analyzed *via* IFEFFIT/SIXPACK. Scanning electron microscopy（SEM, SU8020, HITACHI, Japan）and energy dispersive X-ray spectroscopy（EDS, EMAX, HORIBA）were used to characterize the morphologies of the samples. The particle size of the powder samples was measured on a laser particle size analyzer（Mastersizer 2000, Malvin, England）. The X-ray photoelectron spectroscopy（XPS）measurements were performed on the Axis Ultra DLD（Kratos Analytical Ltd., England）and calibrated to a C 1s electron peak at 284.8 eV. Inductively coupled plasma optical emission spectrometer（ICP-OES）was collected using an Agilent ICPOES730（America）with the power of 1.0 kW. The photoluminescence excitation（PLE）and photoluminescence（PL）were measured using the fluorescence spectrophotometer（FSP920, Edinburgh Instruments, England）combined with a 150 W xenon lamp. The decay curves were excited and detected by a 100 W μF900 lamp and a R928P photomultiplier. Temperature-dependent PL spectra ranging from 300 K to 500 K was measured by the fluorescence spectrophotometer（FLS1000, Edinburgh Instruments, England）with a TAP-02 temperature controller device（Tianjin Orient Koji Co., Ltd, TAP-02, China）. The thermoluminescence（TL）curves were measured at different hating rates from 1 ℃/s to 6 ℃/s with a thermoluminescence meter（FJ427A1, CNCS, China）and the weight of the measured powders was constant（0.05 g）. The TL measurements were carried out immediately after the samples were pre-irradiated for 5 min using a 365 nm UV lamp. The electron paramagnetic resonance（EPR）spectrum was measured by the EPR spectrometer（A300-10/12°, Bruker, Germany）.

3　Results and Discussion

3.1　Structure Characterization

　　The phosphate compound $K_2Zn(PO_3)_4$（named as KZPO）crystallizes in a monoclinic system with space group of Cc（No. 9）, and has the lattice parameters of a = 1.109 41 nm, b = 1.252 15 nm, c = 0.765 97 nm, V = 1.038 94 nm^3. Fig. 1（a）displays the crystal structure of KZPO along with the c-axis direction. Zn atoms have one crystallographic site and are six-coordinated with O atoms to form a distorted ZnO$_6$ octahedra. Besides, PO$_4$ tetrahedra are connected with each other by sharing the corner to present chains in an orderly zigzag manner. Then, a three-dimensional network frame is built up of those polyhedra through sharing common O vertex, where K atoms with two kinds of eight-coordinated sites fill in the spaces enclosed by the polyhedra to balance charge. The structural characteristics demonstrate that KZPO is an ideal matrix to dope transition-metal ions. When Mn ions are doped into KZPO, the XRD patterns of the as-prepared samples are identified and presented in Fig. 1（b）. It can be found that all diffraction peaks are in good accordance with that reported in Inorganic Crystal Structure Database（ICSD # 166829）, indicating that the dopants have a greatly tiny influence on the main crystalline phase.
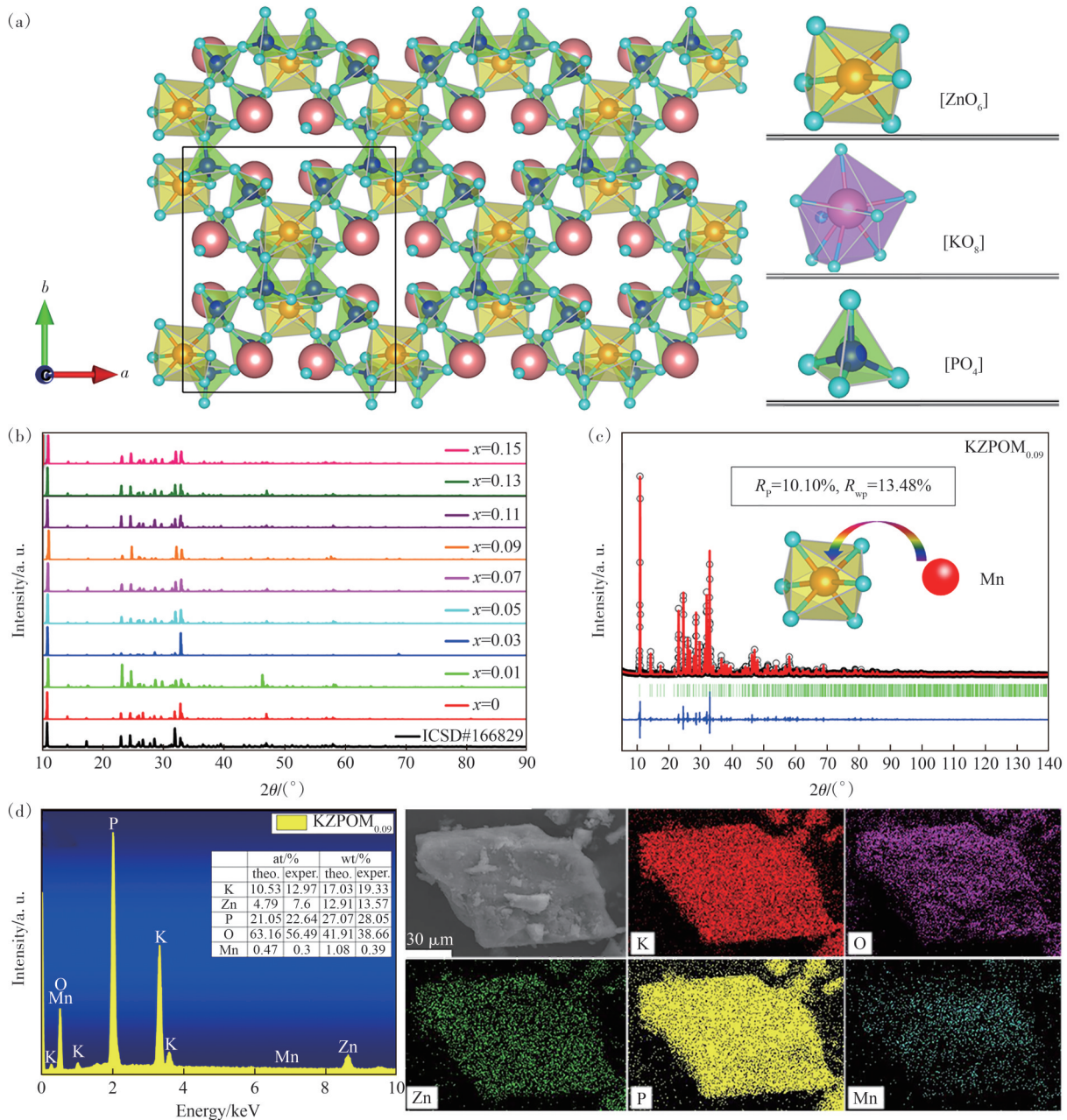
Fig.1 （a）Crystal structure of $K_2Zn(PO_3)_4$. （b）XRD patterns of the $K_2Zn_{1-x}(PO_3)_4 : xMn^{2+}$ （$x = 0-0.15$）. （c）Rietveld refinement result of $K_2Zn_{0.91}(PO_3)_4 : 0.09Mn^{2+}$. The small black circles and the red continuous lines represent the experimental and the calculated values respectively；the blue trace indicates the difference between the experimental and the calculated intensity values；the green vertical bars depict the position of Bragg peaks. （d）SEM image and EDS spectrum of $K_2Zn_{0.91}$-$(PO_3)_4 : 0.09Mn^{2+}$. The inset table lists the atomic and weight percents of all the elements

According to the ionic radius and charge number （CN = 6, $r(Zn^{2+})$ = 0.074 nm, $r(Mn_{LS}^{2+})$ = 0.067 nm, $r(Mn_{HS}^{2+})$ = 0.083 nm, $r(Mn^{4+})$ = 0.053 nm; CN = 8, $r(K^+)$ = 0.151 nm, $r(Mn^{2+})$ = 0.096 nm）, it is preliminarily considered that Mn ions inclined to occupy the Zn^{2+} sites. To further confirm the occupancy preference and local crystal environment of the doping ions, rietveld refinement is performed by using the

structure of KZPO as the initial model with the Topas program[28]. As seen in Fig. 1（c）and Tab. S1-2, the substitution of Mn ions to Zn sites is proved by the reliable agreement converged factors （R_p = 10.10%, R_{wp} = 13.48%, R_{exp} = 4.89%）and theoretically-matched occupancy ratio （8.94%）. In addition, the volume of unit cell of $KZPOM_{0.09}$ is increased to 1.045 20（7）nm^3 and bigger than that of the host

（1.038 94 nm³）, which supports the occupancy preference of high spin-sate Mn²⁺ ions. To sum up, a series of Mn-doped samples all crystallize and do not affect the phase in the regarded concentration range.

　　SEM surface morphology and elemental mapping images of KZPOM₀.₀₉ are tested and exhibited in Fig. 1(d). The bulk particle shows smooth surface and quasi-spherical profile, reflecting the high degree of crystallinity. As seen from EDS spectrum, K, Zn, P, O, and Mn are detected and homogeneously distributed within the selected area. In the inset of the figure, the experimental atomic and weight percents of all elements

are close to their own theoretical values, signifying the successful integration of Mn ions into the host. Besides, Fig. S1(a)–(c) and Fig. S1(d)–(f) also provide the measured results of KZPOM₀.₀₁ and KZPOM₀.₀₅ for a comparison. It is found that the large average particle size of 139.864 μm for KZPOM₀.₀₉ corresponds to a high specific surface area, which could be beneficial to the luminescence performance of materials[29].

3.2　Photoluminescence Properties of KZPOM$_x$

　　The PLE spectrum monitored at 633 nm of KZPOM₀.₀₉ is depicted in Fig. 2(a). The excitation spectrum contains a ligand-metal charge transfer
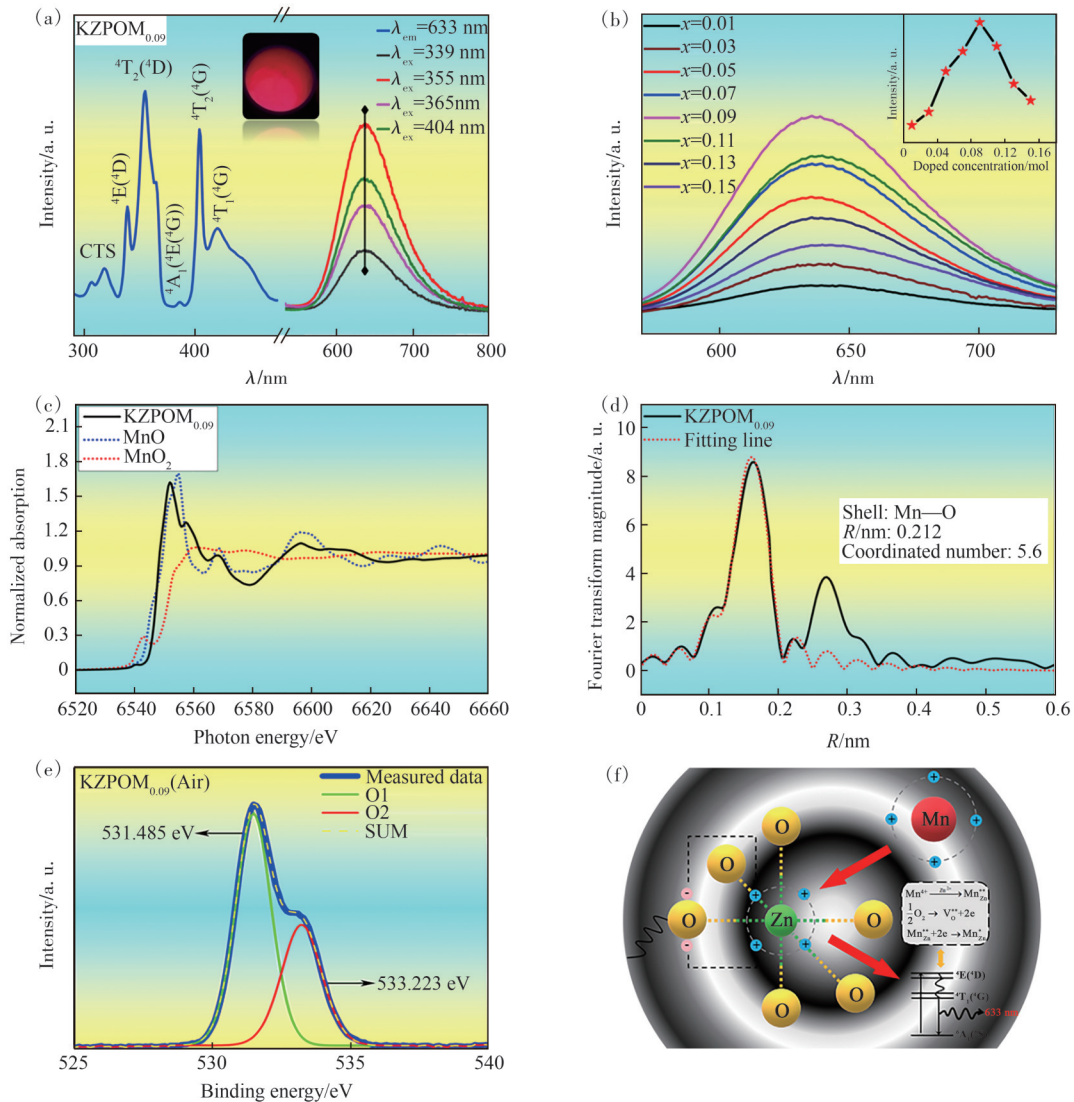

Fig.2　(a) PLE and PL spectra of K₂Zn₀.₉₁(PO₃)₄：0.09Mn²⁺, the inset shows the photograph of KZPOM₀.₀₉ taken by a 365 nm UV-lamp. (b) PL spectra of K₂Zn₁₋ₓ(PO₃)₄：xMn²⁺ (x = 0.01−0.15), the inset shows the relationship between emission intensity and Mn²⁺ concentration. (c) Mn K-edge XANES spectra of KZPOM₀.₀₉, MnO, and MnO₂. (d) The Fourier transforms of Mn K-edge EXAFS spectra and the fitting result of the first neighbor Mn—O coordination of KZPOM₀.₀₉, the inset table is the calculated structural parameters of Mn—O shell. (e) The high-resolution XPS spectrum of O 1s for KZPOM₀.₀₉ (Air). (f) The defect-assisted mechanism diagram of the self-reduction process from Mn⁴⁺ to Mn²⁺ ions

band (LMCT, λ_{ex} = 315 nm) from 3d^5 orbit of Mn^{2+} to 2p^6 orbit of O^{2-}, and several sharp peaks at 339, 355, 365 nm, as well as 404 nm can be attributed to the characteristic d-d electron transitions of Mn^{2+} ions[30-31]. Under the excitation of 355 nm, a broadband red emission centered at 633 nm is observed, which originates from the $^4T_1(^4G) \rightarrow {}^6A_1(^6S)$ transition when Mn^{2+} ions are located in the six-coordinated crystal field circumstance. In the inset of the figure, the emission profile and peak wavelength are independent of the variation of excitation wavelength, indicating that there is one luminescent center in the lattice. As shown in Fig. 2(b), along with the increasing concentration of Mn^{2+} ions, the emission intensity increases gradually until reaching a maximum at x = 0.09 mol, and then decreases because of concentration quenching[32-33]. Fig. S2 displays the CIE chromaticity coordinates diagram of KZPOM$_x$ (0.01 ≤ x ≤ 0.15). It can be found that the chromaticity coordinates of the samples are much closer to that of standard red-light source (x = 0.67, y = 0.33) with the increase of doping content, signify a high color purity emission under the excitation of 355 nm. The lifetime decay curves of KZPOM$_x$ (0.01 ≤ x ≤ 0.13, λ_{ex} = 355 nm, λ_{em} = 633 nm) are measured and exhibited in Fig. S3. All the decay curves can be well fitted by a single-exponential function: $I(t) = I_0 \exp(-t/\tau)$, where $I(t)$ and I_0 refer to the luminescent intensity at time t and 0, respectively. τ is the lifetime of the activator ions[34]. It further proves the conclusion of one luminescent center. In addition, the fitted values gradually decrease from 40.873 9 ms to 39.134 2 ms with the increasing doping concentrations, which is correlated with the exchange-type interaction between Mn^{2+} ions[35].

To further confirm the valence and local crystal environment of doped Mn ions in the lattice, the K-edge X-ray absorption near edge structure (XANES) of KZPOM$_{0.09}$ is adopted and shown in Fig. 2(c). The edge and pre-edge absorption peak of Mn are different from those of raw material MnO$_2$, and consistent with the low-energy peaks (E = 6 503.399 eV) of MnO, which means that Mn ions

exist in a form of bivalence in the lattice[36]. As presented in Fig. 2(d), the fitted average coordinated number obtained from extended X-ray absorption fine structure (EXAFS) spectrum and Fourier transforms is approximated to 5.6 (close to 6 of Zn), verifying the substitution of Mn^{2+} ions to Zn^{2+} sites again[37]. The slightly reduced coordination number indicates the possibility of oxygen vacancy defects (V$_o$), which is further confirmed in the following experiments. Based on the results mentioned above, it is concluded that a self-reduction process from Mn^{4+} to Mn^{2+} ions is realized in the ambient atmosphere for the targeted samples.

According to previous studies, the self-reduction phenomenon is correlated with lattice defects, which would offer extra electrons to adjacent activators to turn them into the low-valence[24,33]. To determine the defect type, ICP-OES is performed and the results are listed in Tab. S3. The experimental weight percent of O is 38.86% in KZPOM$_{0.09}$ and lower than the theoretical value (41.10%). It is illustrated that V$_o$ would be formed in the lattice along with the introduction of Mn ions. Then, high-resolution XPS spectrum of O 1s is further detected and shown in Fig. 2(e), of which the curve can be deconvoluted into two peaks. In addition to the peak belongs to lattice oxygen (531.485 eV), another one with higher binding energy (533.223 eV) should be related to V$_o$[21,38]. In terms of that, a structural schematic model of defect-assisted valence-transfer process of Mn ions is expressed in Fig. 2(f). When Mn^{4+} ions are doped into the lattice, they will occupy the Zn^{2+} sites to form the positively-charged point defects Mn$_{Zn}^{\cdot\cdot}$. Subsequently, the adjacent V$_o$ can provide two unpaired electrons for Mn$_{Zn}^{\cdot\cdot}$ to turn them into the neutral defects (Mn$_{Zn}^{\times}$) and thereby maintain systematic electroneutrality, as shown in the equations in Fig. 2(f).

3.3 Thermal Stability Optimization

The defects generated during the self-reduction process often form trap levels in the forbidden band and influence on the thermal stability. In general, only the deep ones are conductive to the

improvement of thermal stability[39]. Thus, it is essential to construct the trap levels with a suitable depth by defect control for realizing the excellent high-temperature optical performances. Here, a series of samples sintered for different time（17, 24, 36, 48 h）were prepared and the temperature-dependent PL spectra are measured. As depicted in Fig. 3（a）–（d）, it can be found that the luminescent intensities of those phosphors decrease with the increasing temperature. Among them, the sample （24 h）exhibits the optimal thermal stability, and the peak and integrated intensities at 425 K are 84. 4% and 94. 2% of the initial value at room temperature, respectively. Other results for the samples （17, 36, 48 h）are listed in Tab. S4 at the same time. The activation energy（E_a）can be calculated by the Arrhenius equation: $I_T = I_0/[1+\exp(-E_a/kT)]$, where I_T refers to the intensity at certain temperature T, I_0 is the initial intensity, and k is Boltzmann constant[40]. The values are estimated to be 0. 228 eV（17 h）, 0. 157 eV（24 h）, 0. 152 eV （36 h）, and 0. 154 eV（48 h）, respectively. Moreover,

an emission blue-shift from 643 nm to 625 nm with increasing temperatures is observed to appear in all the samples, which is caused by thermally-activated phonon-assisted tunneling effect from the excited states of low-energy emission-band to that of high-energy emission-band [11]. To further discover the effect of oxygen vacancy defects on the thermal stability, a comparison experiment under reducing atmosphere was performed. As shown in Fig. S5, it is interesting to find an anti-thermal quenching phenomenon for the sample sintered in an atmosphere of 10% H_2+90% Ar. Then an electron paramagnetic resonance（EPR）spectrum was used to compare the content of V_o in the samples. The results are shown in Fig. S11. Obviously, the sample sintered in reducing atmosphere possesses a higher resonance signal than that of the sample in ambient atmosphere, which means a higher V_o concentration. It is easy to understand that the samples prepared in a reducing atmosphere have a higher concentration of V_o, and that is why they show a better high-temperature performance.
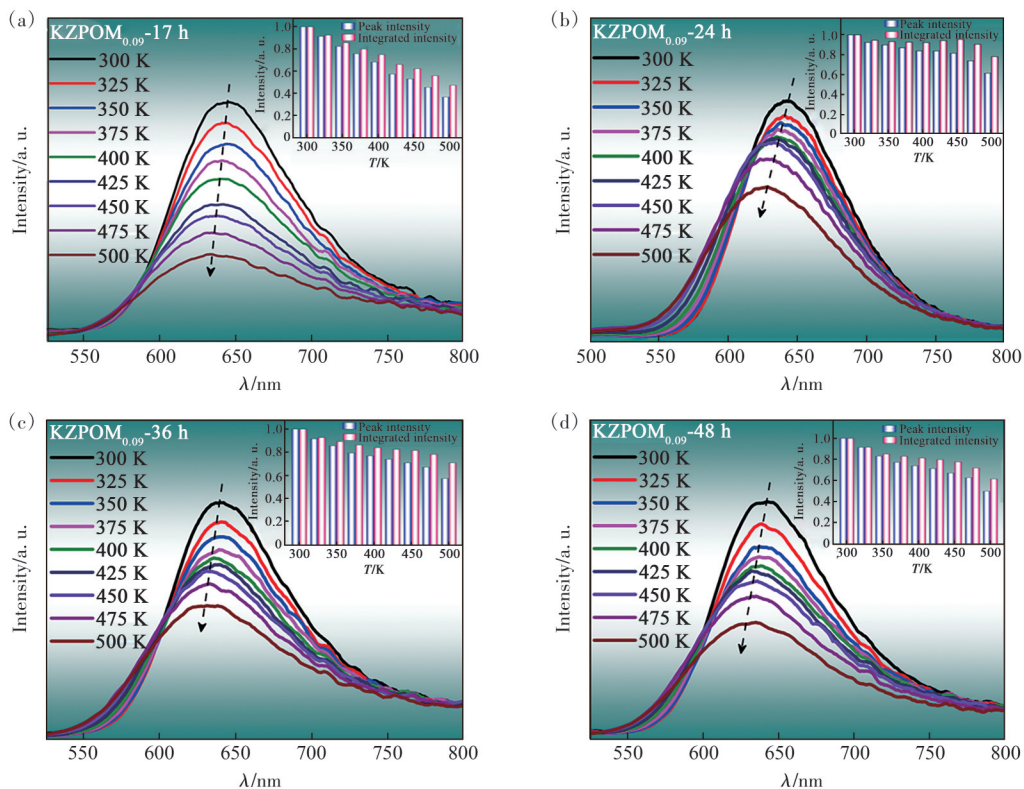

Fig.3　（a）–（d）Temperature-dependent PL spectra of KZPOM$_{0.09}$ with 17, 24, 36, 48 h of sintering time, respectively. The inset shows the dependence of emission spectra on temperature

To further explore the relationship between lattice defects and optical properties, the thermoluminescence is utilized and the spectra are displayed in Fig. 4(a)–(d) and Fig. S6–8. Similarly, the curves are all deconvoluted into three Gaussian peaks at different heating rates（1, 2, 4, 5 ℃/s）, corresponding to different defect positions. Given that, it is indicated that the trap levels exist at specific region of forbidden band in a form of thermally-averaged distribution. From the foregoing, the TQ behavior of phosphors is mainly related to the deep trap levels[41]. Then, the third band peaked at the highest temperature is selected for the further analysis. The depth of trap level can be generally estimated by virtue of Hoogenstraaten formula: $E = -k\ln(\beta/T_m^2)/1/(T_m)$, where k represents the Boltzmann constant, β is the heating rate, and T_m means the corresponding temperature of the TL peak[42]. As seen from Fig. 4(e) and Fig. S9, the values are 0. 926 eV（17 h）, 1. 874（24 h）, 1. 546 eV
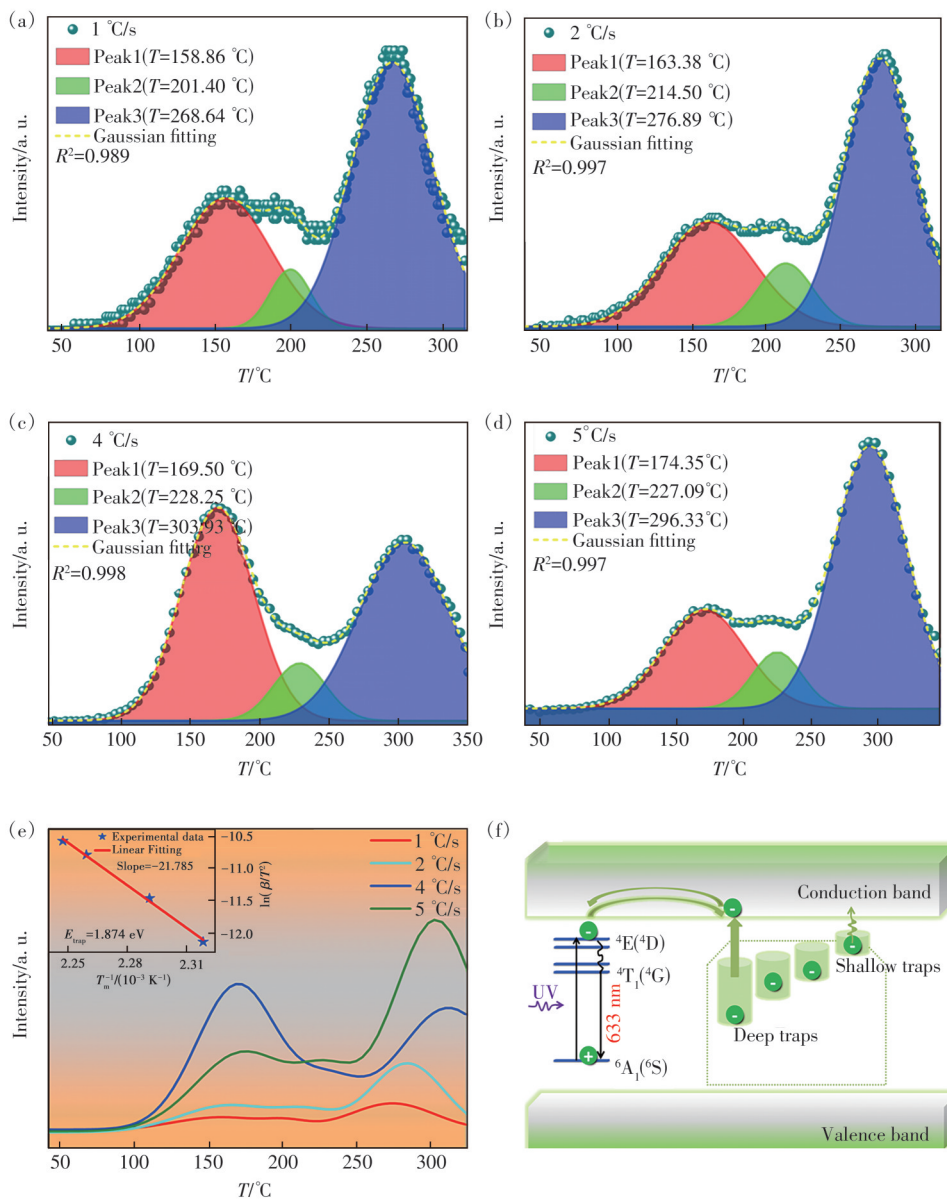

Fig.4 （a）–（d）The TL curves of $K_2Zn_{0.91}(PO_3)_4$：$0.09Mn^{2+}$ sintered for 24 h with different ramping rate of 1 ℃/s, 2 ℃/s, 4 ℃/s, and 5 ℃/s, respectively. （e）The TL curves of $K_2Zn_{0.91}(PO_3)_4$：$0.09Mn^{2+}$ tested at different heating rate when the sintering time is 24 h, the inset shows the Hoogenstraaten plot. （f）The defect-assisted schematic diagram of photoluminescence process

(36 h), and 1. 275 eV (48 h), respectively. The deepest trap levels (E = 1. 874 eV) result in the optimal thermal stability of the sample sintered for 24 h, which embodies the positive response of defect control on luminescent properties and agrees with the conclusions from Fig. 3.

In general, the deeper the trap levels, the more difficult it is for the carriers to escape. Only with the help of external stimulus can the trapped carriers have a possibility to re-participate in the luminescence process, like high temperature. This is why the Mn^{2+}-activated red-emitting phosphors exhibit excellent thermal stability. Accordingly, a schematic diagram of defect-assisted mechanism is proposed in Fig. 4(f). When irradiated by UV light of 355 nm, part of the pumped electrons will be captured by the trap levels, especially the deep ones. Under the stimulus of thermal activation, most of them are released back to the conduction band minimum (CBM) again, and then non-radiative relaxed to the lowest excited state $^4T_1$ of Mn^{2+} ions to re-participate in the radiative transition. The transport process is capable of compensating for the energy loss caused by the non-radiative transition at high temperatures[43-44]. So the deep traps make a significant contribution to enhancing thermal stability, because the carriers are difficult to escape from traps under tiny thermal disturbances at room temperature and only release at high temperatures. The defect control method that changes the crystallization conditions can be applied to other materials to fulfill the requirements of improving optical performance.

4   Conclusion

A series of red-emitting phosphors K_2Zn_{1-x}-$(PO_3)_4$: xMn^{2+} (x = 0. 01−0. 15 mol) were synthesized successfully by the high-temperature solid-state reaction method. Under 355 nm excitation, a broad emission band peaked at 633 nm is observed and considered to originate from the electron transition $^4T_1(^4G) \rightarrow ^6A_1(^6S)$ of Mn^{2+} ions in octahedral crystal field environment. In view of the raw material MnO_2, a self-reduction from Mn^{4+} to Mn^{2+} in the ambient atmosphere is realized in the unit cell, which is benefited from the assistance of V_o. Moreover, through changing the sintering time (17, 24, 36, 48 h) at the same calcinated temperature, the prepared samples show different TQ behaviors, among which the phosphor sintered for 24 h behaves best. The reason is generally related to lattice defects. Based on TL, it is indicated that the trap levels appear in the forbidden band, and part of them are located at the deep positions (E = 1. 874 eV). Those deep trap levels would have a positive effect on the thermal stability. That is, the captured carriers by them can be released to luminescent centers at high temperature, compensating the energy loss caused by non-radiative transitions and thereby improving the thermal stability. This study provides an effective crystallographic method to regulate defect levels and develop novel phosphors with high thermal stability.

Supplementary Information and Response Letter are available for this paper at: http://cjl. lightpublishing. cn/thesisDetails#10.37188/CJL.20240212

References :

[1] SCHUBERT E F, KIM J K. Solid-state light sources getting smart [J]. *Science*, 2005, 308(5726) : 1274-1278.

[2] LUO Z M, QI G Q, CHEN K Y, *et al.* Microwave-assisted preparation of white fluorescent graphene quantum dots as a novel phosphor for enhanced white-light-emitting diodes [J]. *Adv. Funct. Mater.* , 2016, 26(16) : 2739-2744.

[3] LIU X M, XIE W J, LÜ Y, *et al.* Multichannel luminescence properties of mixed-valent Eu^{2+}/Eu^{3+} coactivated $SrAl_3BO_7$ nanocrystalline phosphors for near-UV LEDs [J]. *Inorg. Chem.* , 2017, 56(22) : 13829-13841.

[4] LIU X M, CHEN C, LI S L, *et al.* Host-sensitized and tunable luminescence of $GdNbO_4$: Ln^{3+} (Ln^{3+} = $Eu^{3+}/Tb^{3+}/Tm^{3+}$) nanocrystalline phosphors with abundant color [J]. *Inorg. Chem.* , 2016, 55(20) : 10383-10396.

[5] ZHANG J C, LONG Y Z, ZHANG H D, *et al.* Eu^{2+}/Eu^{3+}-emission-ratio-tunable $CaZr(PO_4)_2$: Eu phosphors synthesized in air atmosphere for potential white light-emitting deep UV LEDs [J]. *J. Mater. Chem.* C, 2014, 2(2) : 312-318.

［ 6 ］ ZHAO M, LIAO H X, NING L X, et al. Next-generation narrow-band green-emitting RbLi(Li$_3$SiO$_4$)$_2$:Eu^{2+} phosphor for backlight display application [J]. Adv. Mater. , 2018, 30(38): 1802489.

［ 7 ］ BACHMANN V, RONDA C, MEIJERINK A. Temperature quenching of yellow Ce^{3+} luminescence in YAG:Ce [J]. Chem. Mater. , 2009, 21(10): 2077-2084.

［ 8 ］ JIAO M M, JIA Y C, LÜ W, et al. Sr$_3$GdNa(PO$_4$)$_3$F:Eu^{2+},Mn^{2+}: a potential color tunable phosphor for white LEDs [J]. J. Mater. Chem. C, 2014, 2(1): 90-97.

［ 9 ］ PARK J K, LIM M A, KIM C H, et al. White light-emitting diodes of GaN-based Sr$_2$SiO$_4$:Eu and the luminescent properties [J]. Appl. Phys. Lett. 2003, 82(5): 683-685.

［10］ HE S G, XU F F, HAN T T, et al. A Mn^{4+}-doped oxyfluoride phosphor with remarkable negative thermal quenching and high color stability for warm WLEDs [J]. Chem. Eng. J. , 2020, 392: 123657.

［11］ RAJENDRAN M, SAMAL S K, VAIDYANATHAN S. A novel self-activated (bluish-green) and Eu^{3+} doped (red) phosphors for warm white LEDs [J]. J. Alloys Compd. , 2020, 815: 152631.

［12］ LI G H, YANG N, ZHANG J, et al. The non-concentration quenching phosphor Ca$_3$Eu$_2$B$_4$O$_{12}$ for WLED application [J]. Inorg. Chem. , 2020, 59(6): 3894-3904.

［13］ CHEN H, WANG Y H. Sr$_2$LiScB$_4$O$_{10}$:Ce^{3+}/Tb^{3+}: a green-emitting phosphor with high energy transfer efficiency and stability for LEDs and FEDs [J]. Inorg. Chem. , 2019, 58(11): 7440-7452.

［14］ DUKE A C, HARIYANI S, BRGOCH J. Ba$_3$Y$_2$B$_6$O$_{15}$:Ce^{3+}: a high symmetry, narrow-emitting blue phosphor for wide-gamut white lighting [J]. Chem. Mater. , 2018, 30(8): 2668-2675.

［15］ CHEN Z, PAN Y X, XI L Q, et al. Tunable yellow-red photoluminescence and persistent afterglow in phosphors Ca$_4$LaO(BO$_3$)$_3$:Eu^{3+} and Ca$_4$EuO(BO$_3$)$_3$ [J]. Inorg. Chem. , 2016, 55(21): 11249-11257.

［16］ ZHU J, YANG M H, CHE Y, et al. Europium (III) doped LiNa$_2$B$_5$P$_2$O$_{14}$ phosphor: surface analysis, DFT calculations and luminescent properties [J]. J. Alloys Compd. , 2020, 822: 153606.

［17］ LIN C C, TSAI Y T, JOHNSTON H E, et al. Enhanced photoluminescence emission and thermal stability from introduced cation disorder in phosphors [J]. J. Am. Chem. Soc. , 2017, 139(34): 11766-11770.

［18］ FANG M H, MENG S Y, MAJEWSKA N, et al. Chemical control of SrLi(Al$_{1-x}$Ga$_x$)$_3$N$_4$:Eu^{2+} red phosphors at extreme conditions for application in light-emitting diodes [J]. Chem. Mater. , 2019, 31(12): 4614-4618.

［19］ JIN Y, FANG M H, GRINBERG M, et al. Narrow red emission band fluoride phosphor KNaSiF$_6$:Mn^{4+} for warm white light-emitting diodes [J]. ACS Appl. Mater. Interfaces, 2016, 8(18): 11194-11203.

［20］ KIM M, PARK W B, LEE J W, et al. Rb$_3$SiF$_7$:Mn^{4+} and Rb$_2$CsSiF$_7$:Mn^{4+} red-emitting phosphors with a faster decay rate [J]. Chem. Mater. , 2018, 30(19): 6936-6944.

［21］ BAI Y X, SUN S J, WU L W, et al. Oxygen vacancy content drives self-reduction and anti-thermal quenching [J]. J. Mater. Chem. C, 2022, 10(11): 4317-4326.

［22］ WU L, SUN S J, BAI Y X, et al. Defect-induced self-reduction and anti-thermal quenching in NaZn(PO$_3$)$_3$:Mn^{2+} red phosphor [J]. Adv. Opt. Mater. , 2021, 9(19): 2100870.

［23］ CHEN H M, BAI Y X, ZHENG L R, et al. Interstitial oxygen defect induced mechanoluminescence in KCa(PO$_3$)$_3$:Mn^{2+} [J]. J. Mater. Chem. C, 2020, 8(19): 6587-6594.

［24］ BAI Y X, WU L W, CHEN Q L, et al. Li$^+$ doping induced zero-thermal quenching in Cs$_3$Zn$_{6-x-y}$B$_9$O$_{21}$:xEu^{3+},yLi$^+$ (0 ⩽ x ⩽ 0.10, 0.06 ⩽ y ⩽ 0.16) [J]. J. Rare Earths, 2023, 41(10): 1478-1486.

［25］ YANG W J, LI J, LIU B D, et al. Multi-wavelength tailoring of a ZnGa$_2$O$_4$ nanosheet phosphor via defect engineering [J]. Nanoscale, 2018, 10(40): 19039-19045.

［26］ AURET F D, GOODMAN S A, LEGODI M J, et al. Electrical characterization of vapor-phase-grown single-crystal ZnO [J]. Appl. Phys. Lett. , 2002, 80(8): 1340-1342.

［27］ PALYANOV Y N, BORZDOV Y M, KHOKHRYAKOV A F, et al. Effect of nitrogen impurity on diamond crystal growth processes [J]. Cryst. Growth. Des. , 2010, 10(7): 3169-3175.

［28］ CHAN T S, LIU R S, BAGINSKIY I. Synthesis, crystal structure, and luminescence properties of a novel green-yellow emitting phosphor LiZn$_{1-x}$PO$_4$:Mn$_x$ for light emitting diodes [J]. Chem. Mater. , 2008, 20(4): 1215-1217.

［29］ WEI Y, YANG H, GAO Z Y, et al. Anti-thermal-quenching Bi^{3+} luminescence in a cyan-emitting Ba$_2$ZnGe$_2$O$_7$:Bi phosphor based on zinc vacancy [J]. Laser Photonics Rev. , 2020, 15(1): 2000048.

［30］ ORGEL L E. Spectra of transition-metal complexes［J］. *J. Chem. Phys.* ，1955，23（6）：1004-1014.

［31］ WU L W，BAI Y X，WU L，*et al*. Analysis of the structure and abnormal photoluminescence of a red-emitting LiMgBO$_3$：Mn^{2+} phosphor［J］. *Dalton Trans.* ，2018，47（37）：13094-13105.

［32］ SONTAKKE A D，VAN BUNNINGEN A J，RABOUW F T，*et al*. Unraveling the Eu^{2+}→Mn^{2+} energy transfer mechanism in w-LED phosphors［J］. *J. Phys. Chem.* C，2020，124（25）：13902-13911.

［33］ ZHENG Z Z，BAI Y X，REN Y J，*et al*. Intrinsic and extrinsic defects build a novel mechanoluminescent phosphor Na$_2$MgGeO$_4$：Mn^{2+}［J］. *J. Mater. Chem.* C，2021，9（10）：3513-3521.

［34］ CHEN H M，WU L W，BO F，*et al*. Coexistence of self-reduction from Mn^{4+} to Mn^{2+} and elastico-mechanoluminescence in diphase KZn（PO$_3$）$_3$：Mn^{2+}［J］. *J. Mater. Chem.* C，2019，7（23）：7096-7103.

［35］ YU B，LI Y C，ZHANG R P，*et al*. A novel thermally stable eulytite-type NaBaBi$_2$（PO$_4$）$_3$：Eu^{3+} red-emitting phosphor for pc-WLEDs［J］. *J. Alloys Compd.* ，2021，852：157020.

［36］ CHEN G P，YU Y R，WU X W，*et al*. Bioinspired multifunctional hybrid hydrogel promotes wound healing［J］. *Adv. Funct. Mater.* ，2018，28（33）：1801386.

［37］ XU K，SUN Y Q，LI X L，*et al*. Fluorine-induced dual defects in cobalt phosphide nanosheets enhance hydrogen evolution reaction activity［J］. *ACS Mater. Lett.* ，2020，2（7）：736-743.

［38］ CHEN H M，LEI Y，LI J J，*et al*. Intense luminescence and good thermal stability in a Mn^{2+}-activated Mg-based phosphor with self-reduction［J］. *Inorg. Chem.* ，2022，61（14）：5495-5501.

［39］ HOERDER G J，SEIBALD M，BAUMANN D，*et al*. Sr［Li$_2$Al$_2$O$_2$N$_2$］：Eu^{2+}：a high performance red phosphor to brighten the future［J］. *Nat. Commun.* ，2019，10（1）：1824.

［40］ TAKAHASHI K，HIROSAKI N，XIE R J，*et al*. Luminescence properties of blue La$_{1-x}$Ce$_x$Al（Si$_{6-z}$Al$_z$）（N$_{10-z}$O$_z$）（*z* similar to 1）oxynitride phosphors and their application in white light-emitting diode［J］. *Appl. Phys. Lett.* ，2007，91（9）：091923.

［41］ KIM J S，PARK Y H，KIM S M，*et al*. Temperature-dependent emission spectra of M_2SiO$_4$：Eu^{2+}（*M* = Ca，Sr，Ba）phosphors for green and greenish white LEDs［J］. *Solid State Commun.* ，2005，133（7）：445-448.

［42］ WANG B，WANG H W，HUANG J H，*et al*. Trap distribution and photo-stimulated luminescence in LaSrAl$_3$O$_7$：Eu^{2+} long-lasting phosphors for optical data storage［J］. *J. Am. Ceram. Soc.* ，2020，103（1）：315-323.

［43］ LIU Z C，ZHAO L，CHEN W B，*et al*. Effects of the deep traps on the thermal-stability property of CaAl$_2$O$_4$：Eu^{2+} phosphor［J］. *J. Am. Ceram. Soc.* ，2018，101（8）：3480-3488.

［44］ YIN Y Z，YANG W H，WANG Z，*et al*. Achieving zero-thermal quenching luminescence in ZnGa$_2$O$_4$：0. 02Eu^{3+} red phosphor［J］. J. *Alloys Compd.* 2022，898：162786.

鹿诗为（2002-），男，山西晋中人，博士研究生，2024 年于南开大学获得学士学位，主要从事应力发光材料与器件的研究。

E-mail：1120240103@mail. nankai. edu. cn

武莉（1976-），女，天津人，博士，教授，博士生导师，2005 年于中国科学院物理研究所获得博士学位，主要从事光电功能材料与器件的研究。

E-mail：lwu@nankai. edu. cn